Frequency dependence and frequency control of microbubble streaming flows

Cheng Wang, Bhargav Rallabandi, and Sascha Hilgenfeldt

Citation: Physics of Fluids **25**, 022002 (2013); doi: 10.1063/1.4790803
View online: http://dx.doi.org/10.1063/1.4790803
View Table of Contents: http://scitation.aip.org/content/aip/journal/pof2/25/2?ver=pdfcov
Published by the AIP Publishing

PHYSICS OF FLUIDS **25**, 022002 (2013)

Frequency dependence and frequency control of microbubble streaming flows

Cheng Wang,[a] Bhargav Rallabandi,[b] and Sascha Hilgenfeldt[c]
Department of Mechanical Science and Engineering, University of Illinois at Urbana-Champaign, 1206 W Green St., Urbana, Illinois 61801, USA

(Received 5 October 2012; accepted 14 January 2013; published online 13 February 2013)

Steady streaming from oscillating microbubbles is a powerful actuating mechanism in microfluidics, enjoying increased use due to its simplicity of manufacture, ease of integration, low heat generation, and unprecedented control over the flow field and particle transport. As the streaming flow patterns are caused by oscillations of microbubbles in contact with walls of the set-up, an understanding of the bubble dynamics is crucial. Here we experimentally characterize the oscillation modes and the frequency response spectrum of such cylindrical bubbles, driven by a pressure variation resulting from ultrasound in the range of 1 kHz $\lesssim f \lesssim$ 100 kHz. We find that (i) the appearance of 2D streaming flow patterns is governed by the *relative* amplitudes of bubble azimuthal surface modes (normalized by the volume response), (ii) distinct, robust resonance patterns occur independent of details of the set-up, and (iii) the position and width of the resonance peaks can be understood using an asymptotic theory approach. This theory describes, for the first time, the shape oscillations of a pinned cylindrical bubble at a wall and gives insight into necessary mode couplings that shape the response spectrum. Having thus correlated relative mode strengths and observed flow patterns, we demonstrate that the performance of a bubble micromixer can be optimized by making use of such flow variations when modulating the driving frequency. © *2013 American Institute of Physics*. [http://dx.doi.org/10.1063/1.4790803]

I. INTRODUCTION

The use of acoustic waves ranging from audible frequency to ultrasound in microfluidic environments (denoted by the term *acoustofluidics*) has enabled versatile manipulation of fluid, as well as of micro/nano-sized objects such as particles, bubbles, and cells.[1] Ultrasound standing waves in the MHz range have been used to trap and separate cell/particles[2] through acoustic radiation forces, which can move the suspended particles/cells to different lateral positions within a laminar stream. Surface acoustic waves (SAWs) of order 100 MHz, which actuate on the fluid as a whole, have demonstrated several practical applications as well, with examples including cell and droplet sorting,[3,4] free surface liquid pumping,[5] and concentration particles.[6] The operation frequency range of the above mentioned methods must be high enough to have acoustic wavelengths comparable to the length scale of cell/particle or microdevices, or to generate momentum flux to move the liquid directly. The potentially undesirable effects are the relatively high power consumption and temperature rise due to heat generation, which may be a concern for biological samples sensitive to temperature. In addition, they both require precise fabrication, such as arrangements of interdigitated structures.[3,4,6]

Acoustic streaming, a classical phenomenon of driving fluid using sound, has found many useful applications at the microscale over the last decade. As pointed out by other researchers,[1,7,8] a

[a]Electronic mail: cwang55@illinois.edu.
[b]Electronic mail: rallaba2@illinois.edu.
[c]Electronic mail: sascha@illinois.edu.

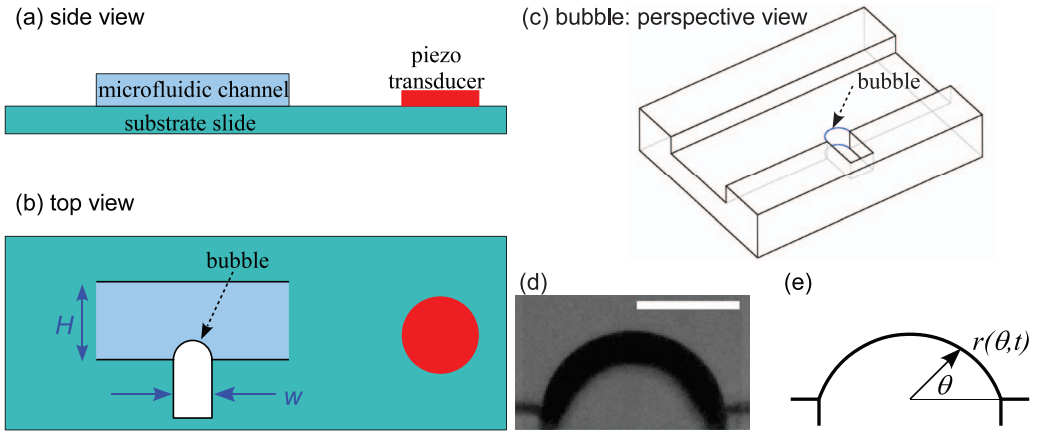

FIG. 1. Schematic of experimental set-up (not to scale): (a) and (b) the side view and top view; (c) a perspective view of the semicylindrical bubble; (d) a snapshot of the undisturbed bubble (scale bar is 50 μm); (e) coordinate system used to measure the bubble shape.

distinction must be made between two general types of streaming: one being a result of attenuation of energy into the fluid during sound propagation (e.g., "quartz wind") and the second being due to the Reynolds stresses within a thin boundary layer (known as boundary-induced *steady streaming*). The former type of acoustic streaming needs to operate in the MHz range to drive steady currents in water.[9] By contrast, boundary steady streaming can be used at a much lower driving frequency to generate steady flows.[10,11] While it is possible to integrate vibrating suspended microstructures[12,13] into a micro-device to induce streaming, such an approach is usually very complex in microfabrication. An alternative way is to induce fluid oscillation over solid objects,[14,15] which is often limited by the low oscillation frequency and small streaming velocity.

Ultrasound-driven oscillating microbubbles serve as excellent actuators to induce microscale steady streaming, offering several advantages such as simple manufacture, easy integration into microfluidic system, and large oscillatory amplitude and thus larger streaming velocity. Protruding air pockets can form spontaneously from indentations in 3D[11,16–18] or from blind side channels in 2D set-ups,[19–22] see Fig. 1. A commercially available piezoelectric transducer can be easily glued anywhere on the substrate to provide excitation, as the direction of acoustic waves is immaterial, in contrast to standing wave or SAW techniques. The compressibility of the bubble enables interface oscillations of large amplitude ϵa with $\epsilon \gtrsim 0.05$, where a is the bubble radius. In the last few years, many microfluidic applications based on bubble streaming have been developed, including mixing enhancement,[19,23] particle sorting and switching,[20,22] and particle focusing and enrichment.[21]

However, a fundamental understanding of microbubble streaming flow lags behind experimental progress. While general theories exist for streaming induced by oscillatory flow over no-slip surfaces,[24] or for bubble-induced streaming in bulk fluid,[25,26] the particular situation in practical devices (Fig. 1) is complicated by the combination of (i) the no-stress bubble boundary condition, (ii) the deformability of the bubble interface, (iii) the contact line between the bubble interface and the wall, and (iv) the necessity of matching the oscillatory boundary layers around the bubble and at the wall. Elder[27] in his pioneering work already described the rich and complex flow patterns from a 3D oscillating hemispherical bubble attached to a wall, submerged in liquids of different viscosities. Tho *et al.* reported experimental investigations of flow fields from 3D hemispherical bubbles confined between two plane walls;[28] in this geometry, qualitative and semiquantitative descriptions emerged,[18,29] but without accounting for problems (iii) and (iv) above. In contrast to these studies, microfluidic devices often have 2D planar geometry due to the lithography-based microfabrication technique, so that cylindrical microbubbles (menisci) are more commonly encountered in practical microfluidics applications.[19–22,30]

Here, we study the oscillations of a cylindrical bubble sandwiched between two plane walls (Fig. 1) and attached to a solid side wall under different driving frequencies, as well as the flow

patterns arising from the bubble dynamics. The secondary steady streaming flow is the time-averaged result of the interaction of first order oscillatory flows, which in turn are caused by the oscillating bubble. To measure the bubble dynamics quantitatively, we use high-speed imaging at up to 100 000 frames per second (fps) to resolve the bubble interface shape in space and time.

II. MATERIALS AND METHODS

A. Experimental set-up

The experimental set-up shares similarities with the ones previously described,[20,21] schematically shown in Fig. 1. The microfluidic channel is made of polydimethylsiloxane (PDMS) using soft lithography.[31] Photoresist (SU-8) is spin-coated on a silicon wafer to 100μm thickness. Through photolithography with a chrome mask, we obtain the master mold in SU-8. The components of PDMS (Sylgard 184, Dow Corning) are well mixed at ratio 10:1, degassed, and poured onto the SU-8 mold to cross-link at room temperature for 24 h. Fully cured PDMS replicas are peeled off from the wafer and bonded to a flat PDMS layer with the help of oxygen plasma treatment. Inlets and outlets are punched using a 1.5 mm Biopsy punch (Premier Uni-Punch) and interfaced through 1/32 in. inner diameter tubing (SmallParts Inc.) for liquid access. The microfluidic device is then bonded at the substrate slide (either glass or polystyrene) after treatment with oxygen plasma. The microfluidic device has a main channel with a depth of $D = 100\mu$m and height in the image plane of $H = 1000\,\mu$m, and a side channel with a opening of $w \approx 80\,\mu$m wide (Fig. 1(b)).

When introducing aqueous glycerol solution (23% glycerol by weight) into the main channel through a syringe pump (PHD Ultra, Harvard Apparatus), an air bubble close to semi-cylindrical shape protruding into the main channel forms in the side channel (Fig. 1(c)). A piezoelectric transducer (thickness 1 mm, diameter 10 mm, Physik Instrumente, Germany) glued to the glass slide provides ultrasonic excitation of the bubble, using sinusoidal signals of frequency $f = 1 - 100$ kHz from a function generator (7075, Hioki, Japan) and amplifier (7500, Krohn-Hite, USA). The device is illuminated by a halogen source (TH4-100, Olympus, USA) for transmitted-light bright-field microscopy.

We use an inverted microscope (IX71, Olympus) with a 20 × or 40 × objective lens, together with a high-speed camera (Phantom v310, Vision Research, USA) to capture top-view images. Polystyrene microparticles of radii $a_p = 0.5 - 1\,\mu$m (Magsphere Inc.) are suspended in a density-matched water-glycerol solution as tracers for streak visualization. Streak photographs are obtained by superposition of typically 1000 successive images at a frame rate of 1000 fps. To study the dynamics of the bubble interface, we capture images of 120 × 80 pixels, at 100 000 fps and with an exposure time of 1 μs (Fig. 1(d)).

B. Data analysis

We vary the driving frequency f from 1.6 kHz to 103.6 kHz, with an increment of $\Delta f = 0.5$ kHz between 1.6 kHz and 25.6 kHz and of $\Delta f = 1$ kHz between 25.6 kHz and 103.6 kHz, while keeping the input driving voltage to the piezoelectric transducer constant. At each frequency, a total of 1000 consecutive images are recorded. The recorded images are imported to freeware ImageJ (NIH, USA),[32] first converted to binary images with proper thresholding, and then the bubble outline in each frame is extracted and saved. We use MATLAB to characterize the bubble outline as a radial function $r(\theta, t)$, measured in polar coordinates from an origin at the center of the side channel opening, as shown in Fig. 1(e). We will show that information about the bubble motion in the radial-azimuthal plane (Fig. 1(e)) is sufficient to explain its behavior, i.e., oscillations in the direction of the axis of the cylindrical bubble have negligible effect and both the bubble surface oscillations and the resulting flow fields can be understood as two-dimensional dynamics in the radial-azimuthal plane. Below, we present both experimental evidence and theoretical justification for this treatment of the problem as an oscillating 2D bubble.

The shape of the initially undisturbed bubble is described by $r_0(\theta, 0)$. The angle-dependent amplitude of the bubble is then characterized by $\Delta r(\theta, t) = r(\theta, t) - r_0(\theta, 0)$. Even though the

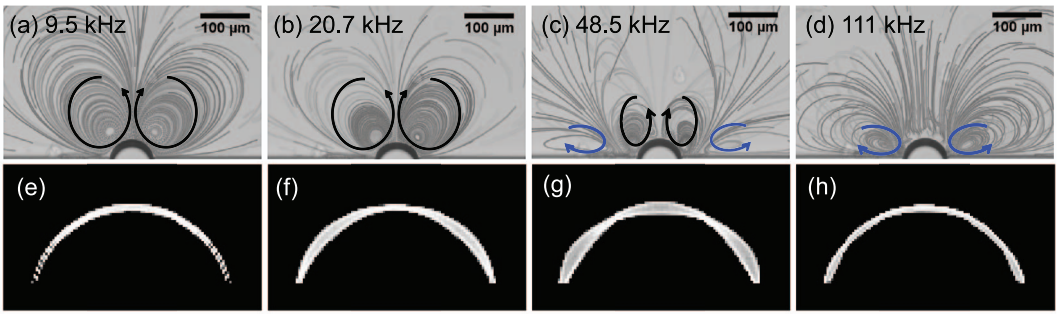

FIG. 2. Bubble streaming flow patterns at different driving frequencies, with arrows indicating the orientations of the vortices. Outline of oscillatory bubble superposed over one cycle at different frequencies (e) 9.6 kHz, (f) 20.6 kHz, (g) 48.6 kHz, and (h) 100.3 kHz.

camera sampling rate is almost the same as the higher driving frequencies $f \sim 100\,\text{kHz}$, the very short exposure time ($1\,\mu\text{s}$) and carefully chosen driving frequencies allow us to improve the time resolution using stroboscopic techniques. For each frequency, we use the middle 500 frames of the captured images for analysis. We then determine the mode amplitude and phase angle by performing Fourier decomposition according to

$$\Delta r(\theta, t) = a \sum_{n=0} a_n \cos(2n\theta) \sin(\omega t + \phi_n), \tag{1}$$

where $\omega = 2\pi f$ is the angular frequency, a_n are the dimensionless mode amplitudes, and ϕ_n the phase angles. The decomposition into cosines is suggested by the symmetry of the interface and the presence of the wall.

III. RESULTS AND DISCUSSION

A. Flow patterns at different driving frequency

When changing driving frequency f in the range of 1.6 kHz to over 100 kHz, we have observed a succession of different flow patterns, as shown in Fig. 2. At lower frequencies (Figs. 2(a) and 2(b)), there are two symmetric vortices above the bubble, drawing liquid towards the bubble and pushing liquid upwards along the pole of the bubble. We denote this pair as "*fountain*" vortices or loops. This flow pattern has been described as the "generic" streaming pattern near an interface, both in the present 2D set-up[19,20] and (as an analogous toroidal vortex loop) for 3D hemispherical bubbles.[11,18,27] As f increases in our set-up, a second pair of vortices is observed to appear, with orientation opposite ("*anti-fountain*") to the first pair (see Fig. 2(d)). With even higher driving frequencies, the "anti-fountain" vortices dominate over the "fountain" vortices (see Fig. 2(d)), reversing the far-field flow pattern. In Figs. 2(e)–2(h), we show the corresponding outlines of the bubble movement by superimposing high-speed images over one cycle near the frequencies of the streak images. At frequency $f \approx 10\,\text{kHz}$, the outline shows a single crescent (antinode) near the pole of the bubble. With increased f, more nodes and anti-nodes appear, see Figs. 2(f) and 2(g). At even higher f, the outline seems to have a uniform oscillation along the entire bubble. The different node patterns indicate the presence of frequency-dependent bubble oscillation (shape) modes. For a free bubble driven by a time-varying pressure field, the monopole is excited most effectively and separately from any shape modes. For a bubble located at the side channel opening, however, shape and volume modes have to be excited together to accommodate pinning of the contact line. Note that this pinning may be weak: There may be some mobility of the contact line, but because it is located near the corner connecting the horizontal wall and the side channel wall, its location changes little even for significant bubble oscillations. In Sec. III B, we present quantitative measurements of these mode contributions.

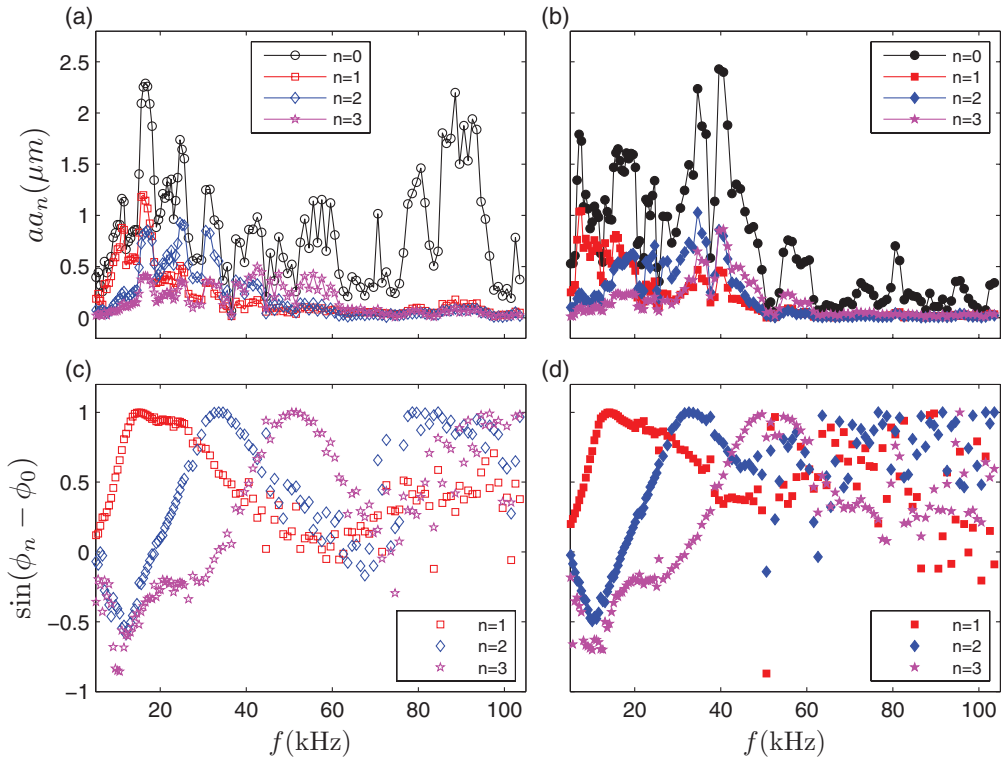

FIG. 3. Measured dimensional mode amplitude $a\,a_n$ (a) and (b), and phase which is represented in terms of $\sin(\phi_n - \phi_0)$ (c) and (d). Open symbols are for the glass substrate, filled symbols for the polystyrene substrate.

B. Mode amplitude and phase

We plot the amplitude of the first four ($n = 0, 1, 2, 3$) modes for a microfluidic device mounted on a glass substrate in Fig. 3(a); Fig. 3(c) shows the difference of phase angles between the shape modes $n > 0$ and the volume mode $n = 0$, through the term $\sin(\phi_n - \phi_0)$. The bubble amplitude response curves in Fig. 3(a) are jagged, while the phase difference shows a smooth change as f is varied (Fig. 3(c)). The strong variations in the amplitude spectrum can be explained by the actual driving pressure levels acting on the bubble, which depend on both the characteristic resonances of the piezoelectric transducer and the characteristic response of the entire fluidic set-up, changing with its material composition and geometry. In an earlier experimental study, Tho *et al.* measured the pressure level using a hydrophone and found a strongly nonlinear acoustic pressure amplitude as a function of excitation frequency.[28] In other words, the non-smooth amplitude curve is attributed to a non-constant driving pressure, though the driving voltage to the piezoelectric transducer is kept constant.

We demonstrate the dependence on material composition by measuring the bubble response with a different set-up where the substrate slide is made of polystyrene. The details of the resulting amplitude spectra (Fig. 3(b)) are very different from Fig. 3(a). By contrast, when comparing the measured phase angles Figs. 3(d) and 3(c), we observe almost identical phase spectra, indicating these as intrinsic characteristics of the bubble motion.

Encouraged by the universal spectra of relative phases, we proceed to analyze the analogous amplitude property, i.e., the *relative* amplitude of each mode normalized by that of the volume mode $\overline{a}_n = a_n/a_0$. In Fig. 4(a), $\overline{a}_n$ is plotted for both the microfluidic devices mounted on the glass substrate and the polystyrene substrate, respectively. The curves are in very close agreement, indicating that the quantity $\overline{a}_n$ can be used to describe the intrinsic bubble response regardless of the fluidic set-ups. This normalization strategy thus allows for meaningful comparison of data across set-ups and reveals a much simpler, robust resonance structure. We note that the monopole amplitude is always

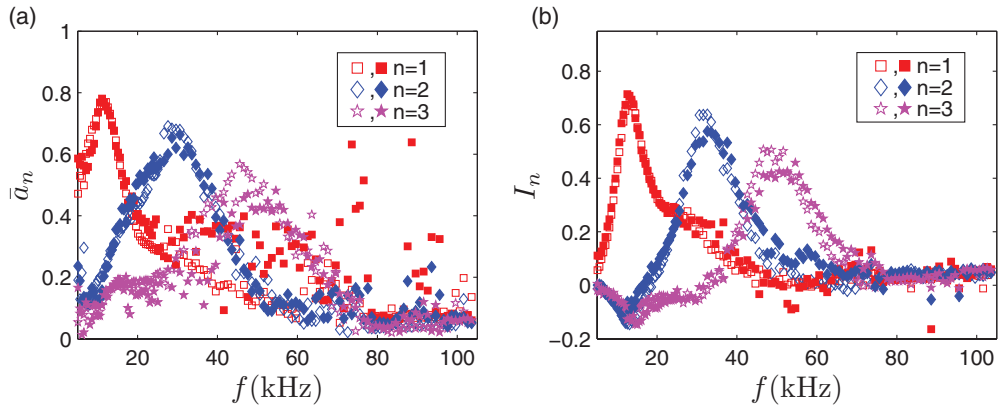

FIG. 4. Normalized mode amplitudes $\bar{a}_n$ with respect to monopole (a) and relative streaming strength I_n (b). Open symbols are for the glass substrate, filled symbols for the polystyrene substrate.

the largest for all driving frequencies, while the higher order modes show distinct peaks, around 12 kHz for $n = 1$, 30 kHz for $n = 2$, and 45 kHz for $n = 3$, respectively. However, it must be pointed out that these peaks are not conventional resonant frequencies, which are defined as peaks under a constant driving pressure (note that direct measurement of driving pressure with hydrophones is possible in cm-scale fluid chambers,[28] but is impractical inside a sub-mm microchannel). The relative amplitudes and phases thus emerge as important parameters to characterize the bubble behavior and subsequently predict the streaming flow, as discussed below.

C. Relative streaming strength and flow patterns

Steady streaming through Reynolds stresses at boundary layers can always be interpreted as a second-order effect in the amplitudes of first-order oscillatory flows, i.e., in our case, steady streaming flow components are proportional to quadratic terms of mode amplitudes. Nominally, one would expect the term $\propto a_0^2$ to be the strongest contribution on account of the large a_0 values, but a pure (radial) volume oscillation does not lead to any steady streaming.[26] Therefore, the dominant streaming terms should be those resulting from the interaction of the volume mode and an $n > 0$ shape mode. The velocity scale of this *mixed-mode* streaming can be shown to be proportional to $a_0 a_n \sin(\phi_n - \phi_0)$, i.e., the phase shift between the modes is important. Making use instead of our normalized amplitudes, we conclude that $I_n \equiv \bar{a}_n \sin(\phi_n - \phi_0)$ is a measure of bubble streaming intensity due to the interaction between higher order and monopole oscillatory flows.

We plot I_n for the microfluidic devices mounted on glass and polystyrene substrates in the same graph, Fig. 4(b). The data from both set-ups again coincide, indicating that intensity I_n displays resonance peaks intrinsic to a bubble of a given radius. A resonance spectrum is observed: as f is increased, I_1 has the largest magnitude from between a few kHz to about 25 kHz and peaks around 15 kHz. Between 25 kHz and 40 kHz, I_2 is seen to have a larger contribution, with a peak at about 30 kHz, while I_3 peaks around 50 kHz. The streaming flow depends on other modes of streaming as well, e.g., on contributions like $\bar{a}_1 \bar{a}_2 \sin(\phi_2 - \phi_1)$. However, these are typically small, because of the small prefactors (we find $\bar{a}_1 \bar{a}_2 \sin(\phi_2 - \phi_1) \lesssim 0.2$) and also because higher-order streaming contributions decay faster with distance from the bubble.

In general, higher order mixed streaming tends to have more complex flow structure near the bubble surface. In order to visualize the finer flow structures of the streaming flow, particularly near the bubble surface, we use smaller tracers ($a_p = 0.5\,\mu$m) and a 40 $\times$ objective lens. Streak photographs of four different f are shown in Fig. 5. A closer examination of Figs. 4(b) and 5 shows a change of flow patterns with varying prominence of different I_n. At low frequency in Fig. 5(a), the predominant two "fountain" vortices flow structure is a result of the streaming from the $n = 0$ and $n = 1$ modes. As f is increased to around 30 kHz, a second pair of small "anti-fountain" appears near the pole, a result of stronger $n = 0$ and $n = 2$ mode streaming (Fig. 5(b)). Further increase of f

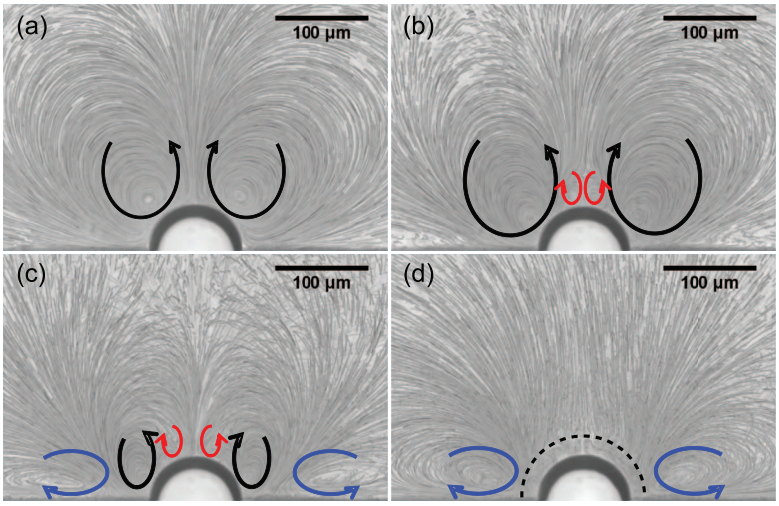

FIG. 5. Streaming flow patterns with small tracer particles and better spatial resolution: (a) 14.4 kHz, (b) 30.9 kHz, (c) 48.4 kHz, and (d) 93.4 kHz (note small vortices between the dashed line and the bubble surface).

induces even more complex structures near the bubble surface and at the same time another pair of "anti-fountain" vortices emerges from the wall (Fig. 5(c)). At the highest f, the flow near the bubble has many small vortices (between the dashed line in Fig. 5(d) and the bubble surface), while the "anti-fountain" near the wall grows larger and dominates the whole flow field. We have verified[20,21] that these flow patterns change little in the direction perpendicular to the views presented, i.e., the flow is 2D in character. This is surprising at first glance, as the axial length of bubble D is not much greater than its diameter w. We will develop and justify the 2D approach in Secs. III D and III E.

D. Theory of cylindrical bubble oscillations

The flow patterns and their symmetries depend on the resonance structure of the bubble shape oscillations visible in Fig. 4. The resonance behavior of free bubbles has long been known,[33,34] and other work has treated oscillations of hemispherical droplets[35,36] and hemispherical bubbles on solid supports.[37] In many microfluidic devices, as in ours, the bubble is confined by two parallel supporting walls to which it is attached via large contact areas, thus assuming a cylindrical symmetry (experimentally we can verify that these contact areas are immobile). It is additionally pinned to rigid walls by means of two contact lines that span the depth of the bubble along the y-axis (Figure 6(a)). This practically relevant case, i.e., that of a bubble whose interface is part of a cylinder, attached to a wall along contact lines, has not previously been treated. We will see that the resonance features

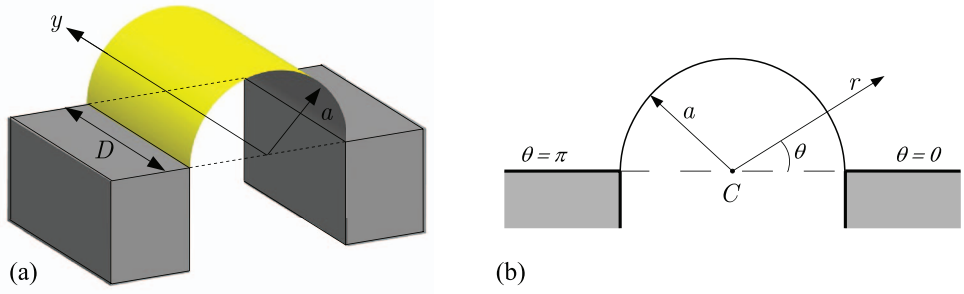

FIG. 6. (a) Geometry of the cylindrical bubble confined between plates a distance D apart. (b) Coordinate system of the 2D geometry used in the calculation of bubble oscillations.

of the bubble oscillation can be understood within an asymptotic theory framework that accounts for the coupling of azimuthal modes through the boundary conditions.

We consider here an idealization of the experimental set-up: a cylindrical bubble of radius a confined between parallel plates of distance D and pinned to a wall by means of two contact lines, as shown in Fig. 6. We will assume that this wall is smooth, rigid, and no-slip, and that the contact lines between the bubble surface and the wall remain stationary. A polar coordinate system coaxial with the bubble is used, with the walls at $\theta = 0$ and $\theta = \pi$. We consider the situation where the surface of the bubble undergoes oscillations at a single angular frequency ω with a characteristic dimensionless amplitude ϵ, producing a characteristic oscillatory velocity $U = \epsilon a\omega$ of the surrounding fluid.

For $\epsilon \ll 1$, the flow, to leading order, is described by the linearized Navier-Stokes equations, and being driven by surface oscillations of the bubble, shares the same angular frequency ω. We first neglect axial oscillations of the bubble surface, and therefore approximate the flow field by a planar flow and the bubble interface by a line in the (r, θ) plane (Fig. 6(b)). Using a, ω^{-1}, and U as characteristic scales for length, time, and velocity, we introduce a dimensionless stream function $\psi(r, \theta, t)$ that gives the components of velocity in the plane $u_r = r^{-1}\partial\psi/\partial\theta$ and $u_\theta = -\partial\psi/\partial r$. The linearized vorticity equation may then be written as

$$(\nabla^2 - \alpha^2)\nabla^2\psi = 0, \tag{2}$$

where $\alpha = (1 + i)/\delta$, with $\delta = a^{-1}\sqrt{2\nu/\omega}$ being the Stokes boundary layer thickness.

We assume that the bubble interface $R(\theta, t) = 1 - i\epsilon\zeta(\theta)e^{it}$ is impermeable and stress-free. These boundary conditions may be imposed, to leading order in ϵ, at the mean position of the bubble[26] and read

$$\left.\begin{aligned} \epsilon\frac{1}{r}\frac{\partial\psi}{\partial\theta} &= \dot{R} = \epsilon\,\zeta(\theta)e^{it} \\ \frac{\partial^2\psi}{\partial r^2} - \frac{1}{r}\frac{\partial\psi}{\partial r} - \frac{1}{r^2}\frac{\partial^2\psi}{\partial\theta^2} &= 0 \end{aligned}\right\} r = 1. \tag{3}$$

In addition, the flow must be no-slip on the rigid walls at $\theta = 0$ and $\theta = \pi$, given by

$$\frac{1}{r}\frac{\partial\psi}{\partial\theta} = \frac{\partial\psi}{\partial r} = 0 \;: \qquad \theta = 0,\ \pi. \tag{4}$$

Separable solutions to (2) of azimuthal wave number k are readily obtained as

$$\psi_k(r, \theta) = \hat{\psi}_k(r)\exp ik\theta\, e^{it} = \left(\frac{C_k}{r^k} + D_k K_k(\alpha r)\right)\exp ik\theta\, e^{it}, \tag{5}$$

where k may assume any complex value with a non-negative real part. The corresponding bubble shape ζ is given by the kinematic boundary condition as

$$\zeta_k(r, \theta) = \hat{\zeta}_k(r)\exp ik\theta\, e^{it}, \quad \text{where} \quad \hat{\zeta}_k(r) = ik\hat{\psi}_k(r). \tag{6}$$

The modified Bessel function of the second kind $K_k(\alpha r)$ is an exponentially decaying vortical solution that persists only in the boundary layer, while the algebraically decaying term in (5) represents the potential flow solution, with a corresponding potential

$$\phi_k(r, \theta) = -i\frac{C_k}{r^k}\exp ik\theta\, e^{it}. \tag{7}$$

If, by comparison, we take axial oscillations (along the coordinate y) into account as well, we find potential flow solutions by separation of variables[38,39] as

$$\phi_{km}(r, \theta, y) = K_k(mr)\exp ik\theta\ \exp imy\, e^{it}, \tag{8}$$

where m is the dimensionless axial wave number. This solution replaces the power-law terms (7) for $m \neq 0$. Note that the modified Bessel function decay in (8) is much stronger as r grows away from the bubble surface, becoming exponential for $mr > 1$. As the smallest non-zero m is $m = 2\pi a/D$ (at least one axial wavelength must fit along D), this is fulfilled at even a fraction of a bubble radius

away from the surface. The oscillatory flow field away from the bubble is therefore dominated by the two-dimensional flow solutions given in (5). Additionally, we will show below that the expected excitation amplitude of the axial oscillation modes is significantly smaller than that of the azimuthal modes.

E. Theory of bubble resonance

While the general solutions (5) satisfy the kinematic boundary condition, determining coefficients C_k and D_k that satisfy both the stress-free condition at the bubble and the no-slip condition at the wall is not trivial. We address this problem by recognizing[6] that by temporarily relaxing the zero-tangential velocity at the boundary condition at the wall, the general solution (5) simplifies to a Fourier sine series, to which the no-stress boundary condition may be applied separately for each mode k, due to orthogonality properties of the series. Assuming symmetry of the bubble shape about $\theta = \pi/2$, we have a general solution ψ_b to this modified problem

$$\psi_b(r,\theta) = \sum_{n=0}^{\infty} A_n \left(\frac{c_{2n}}{r^{2n}} + d_{2n} K_{2n}(\alpha r) \right) \sin 2n\theta \, e^{it} \tag{9}$$

with c_k and d_k given by

$$c_k = \frac{1}{k} - d_k K_k(\alpha) \quad \text{and} \quad d_k = -\frac{2(k+1)}{\alpha^2 K_{k-2}(\alpha) + 2k\alpha K_{k-1}(\alpha)}, \tag{10}$$

and the corresponding bubble shape $\zeta_b = \sum A_n \cos 2n\theta$. We have, in (9), constructed a general slip solution that is ignorant of viscous effects near the wall, which may then be employed as leading order "outer solution" in a matched asymptotic expansion. The expansion in integer k reinforces the conclusion that slowly decaying solutions with exclusively azimuthal variation will dominate fast-decaying solutions with axial variation and result in 2D flow, as observed in experiment.

We now invoke the well known solution for a viscous oscillatory flow near a wall[7] in the limit of thin boundary layers ($\delta \ll 1$), composed of a wall boundary layer structure driven by an oscillatory slip. The stream function ψ_w in the boundary layer over the wall at $\theta = 0$ is given as

$$\psi_w(r,\xi) = \delta \, r \, v(r) \left\{ \xi - \frac{1}{r(1+i)} \left(1 - e^{-(1+i)\xi r} \right) \right\} e^{it} + O(\delta^3), \tag{11}$$

with $\xi = \theta/\delta$ a rescaled azimuthal coordinate and $v(r)\, e^{it}$ the oscillatory slip velocity at the edge of the wall boundary layer. Asymptotic matching of the wall boundary layer solution to the outer solution as $\xi \to \infty$, together with the symmetry of the bubble oscillations about $\theta = \pi/2$, enforces that k is a non-negative even integer. We may then write for the slip velocity

$$v(r) = \sum_{n=0}^{\infty} 2n A_n \frac{c_{2n}}{r^{2n+1}} = \sum_{n=0}^{\infty} \frac{A_n}{r^{2n+1}} + O(\delta^2), \tag{12}$$

where A_n are the (generally complex) weights of the different angular components of the flow field and the approximation results from a δ-expansion of (10).

We have so far excluded the corner regions near the contact lines, in which the bubble and wall boundary layers overlap and where the wall boundary layer solution might become modified by radial gradients warranted by the no-stress bubble surface. However, an expansion in orders of δ of (5) verifies that the bubble boundary layer terms are absent up to the order to which the wall boundary layer solution (11) is valid, which enables the extension of (11) into the corner regions up to the bubble surface. We must still address any potential modification of the stress-free condition at the bubble surface that could have been introduced by this extension. The tangential stress in the corner is readily calculated from (3) and (11) as

$$\frac{1}{\delta^2} \left(\delta^2 \frac{\partial^2}{\partial r^2} - \delta^2 \frac{1}{r} \frac{\partial}{\partial r} - \frac{1}{r^2} \frac{\partial^2}{\partial \xi^2} \right) \psi_w \Big|_{r=1} = \frac{1+i}{\delta} v(1) e^{-(1+i)\xi} + O(\delta). \tag{13}$$

Clearly, if the bubble surface is everywhere stress free, it must be true that

$$v(1) \sim \sum_{n=0}^{\infty} A_n = O(\delta^2). \tag{14}$$

We will henceforth ignore the bubble boundary layer for further calculations, but note its importance in maintaining a stress-free bubble surface. Using (5), (11), and (12), a uniformly valid solution for the oscillatory velocity field is then given as

$$\boldsymbol{u}(r,\theta) \sim \sum_{n=0}^{\infty} \frac{A_n}{r^{2n+1}} \Big[\left\{ \cos 2n\theta - \left(e^{-\alpha\theta r} + e^{-\alpha(\pi-\theta)r} \right) \right\} \hat{\boldsymbol{e}}_r + \sin 2n\theta \, \hat{\boldsymbol{e}}_\theta \Big] e^{it}. \tag{15}$$

Using the kinematic condition in (3), the bubble shape is described by

$$\zeta(\theta) = \sum_{n=0}^{\infty} A_n \left[\cos 2n\theta - \left(e^{-\alpha\theta} + e^{-\alpha(\pi-\theta)} \right) \right]. \tag{16}$$

It is worth noting that (16) implies pinned contact lines simply by virtue of the walls being strictly no-slip.

In the linear limit, the pressure field is a harmonic function and plays the role of a velocity potential in the bulk of the fluid, where the flow is irrotational. Using a pressure scale $\epsilon \rho a^2 \omega^2$, the oscillatory pressure in the liquid is given by

$$P^e(r,\theta,t) = i\epsilon\rho a^2\omega^2 \left(p^* + A_0 \log \frac{R_\infty}{r} + \sum_{n=1}^{\infty} \frac{A_n}{r^{2n}} c_{2n} \cos 2n\theta \right) e^{it}. \tag{17}$$

Note that the pressure at infinity diverges logarithmically as a consequence of the assumption that the flow is two-dimensional and may be regularized by assuming weak gradients in the axial direction. For the purpose of this discussion, we retain (17), and replace the limit $r \to \infty$ by $r \to R_\infty$, assuming that R_∞ is large enough that the pressure at $r = R_\infty$ associated with the surface modes is negligible. p^* is then the non-dimensional uniform oscillatory pressure that persists at infinity and may be externally imposed in the case of a long wavelength forcing, as in our experiments.

We now proceed to describe the bubble interfacial dynamics, and thus coefficients A_n, as functions of the frequency of oscillation and the physical parameters of the system. At the bubble interface, the normal stress balance yields $\sigma^e_{nn} - \sigma^i_{nn} - \Gamma\kappa = 0$, where σ^e_{nn} and σ^i_{nn} are normal stresses on the interface due to the external and internal fluids, respectively, κ is the sum of the principal curvatures of the interface, and Γ is the surface tension coefficient of the interface. To leading order in ϵ, the unit normal at the surface is given by the unit vector in the radial direction and we have $\sigma^e_{nn} = \sigma^e_{rr} = -P^e + \tau_{rr}$, where P^e is external fluid pressure at interface ($\zeta = 0$) and $\tau_{rr} = \epsilon\omega\mu\, \partial u_r/\partial r|_{\zeta=0}$ is the interfacial viscous normal stress due to the external fluid.

For a typical air bubble in water, the density and the dynamic viscosity of the interior gas is much smaller than the exterior liquid, so that stresses due to the gas dynamics may be neglected and the internal oscillatory pressure P^i follows the radius dynamics via a polytropic law of exponent η, $P^i \propto R^{-3\eta}$.

The curvature κ of the bubble interface may be calculated using (16), which yields to leading order in ϵ

$$\kappa(\theta,t) = \frac{i\epsilon}{a} \left[\sum_{n=0}^{\infty} A_n (4n^2 - 1) \cos 2n\theta + (\alpha^2 - 1) \left(e^{-\alpha\theta} + e^{-\alpha(\pi-\theta)} \right) \sum_{n=0}^{\infty} A_n \right] e^{it}. \tag{18}$$

If thermal and acoustic effects are negligible, the normal stress balance, rewritten as $P^i - P^e + \tau_{rr} - \Gamma\kappa = 0$, gives the dynamical equation describing the linear oscillations of the bubble, which may be recast as

$$-\omega^2 \mathbb{P}(\theta) + 2i\gamma\Omega\omega \mathbb{T}(\theta) + \Omega^2 \mathbb{K}(\theta) + \Omega_v^2 A_0 = \omega^2 p^*, \tag{19}$$

where $\Omega = \sqrt{\Gamma/\rho a^3}$, $\gamma = \mu/\sqrt{\rho a \Gamma}$, and $\Omega_v = \sqrt{\pi\eta P_0/\rho S_0}$.

Ω is an angular frequency scale for surface mode resonance and Ω_v is a 2D Minnaert frequency describing volume resonance of a gas bubble with a rest cross-sectional area of S_0. $\mathbb{P}(\theta)$, $\mathbb{T}(\theta)$, and $\mathbb{K}(\theta)$ are the normal stress contributions of the pressure, viscous damping, and curvature, respectively, and are given by

$$\begin{aligned}
\mathbb{P}(\theta) &= A_0 \log R_\infty + \sum_{n=1}^{\infty} A_n \left(\frac{1}{2n} - i\,\delta^2(2n+1) \right) \cos 2n\theta, \\
\mathbb{T}(\theta) &= \sum_{n=0}^{\infty} A_n(2n+1)\Big[\cos 2n\theta - \left(e^{-\alpha\theta} + e^{-\alpha(\pi-\theta)} \right) \Big] \\
&\quad -\alpha \left(\theta e^{-\alpha\theta} + (\pi-\theta) e^{-\alpha(\pi-\theta)} \right) \sum_{n=0}^{\infty} A_n, \\
\mathbb{K}(\theta) &= \sum_{n=0}^{\infty} A_n(4n^2-1)\cos 2n\theta \\
&\quad +(\alpha^2-1)\left(e^{-\alpha\theta} + e^{-\alpha(\pi-\theta)} \right) \sum_{n=0}^{\infty} A_n.
\end{aligned} \tag{20}$$

The $O(\delta^2)$ correction to the pressure produces terms comparable in size to the leading order damping terms in the bulk of the fluid, via $\omega^2\delta^2 = 2\gamma\omega\Omega$, and is therefore retained. The last term of $\mathbb{T}(\theta)$ is negligible if $\gamma \ll 1$, considering (14). Note however, that the boundary layer terms in curvature term $\mathbb{K}(\theta)$ may be sizable due to the prefactor of α^2, in spite of (14).

If axial oscillations are again considered, it can be shown that the damping coefficient $\gamma_n = \gamma(2n + 1)$ for the nth azimuthal mode is modified in the presence of an oscillation of axial wavenumber m to

$$\gamma_n(m) = \gamma \frac{m}{2} \frac{K_{2n-2}(m) + 2K_{2n}(m) + K_{2n+2}(m)}{K_{2n-1}(m) + K_{2n+1}(m)}. \tag{21}$$

This reduces to γ_n as $m \to 0$, but bearing in mind that m is at least $2\pi a/D$, we find for our experimental parameters that even this lowest axial wave number leads to about five times larger damping as compared to $m = 0$. Therefore, axial oscillations not only induce fast-decaying flow fields, but the amplitude of these flow fields is, at equal excitation, much smaller to start with when compared to the purely azimuthal modes. This further justifies the 2D model and rationalizes the observed planar flow fields.

The radius dynamics are described by the component of (19) that is independent of θ, and involves the forcing pressure p^* and the constant R_∞, which was introduced due to the planar flow assumption. They are, however, irrelevant in the calculation of the surface mode amplitudes relative to the radial mode. Formally, we evaluate a Fourier cosine series of (19) and consider only those components that have explicit θ dependences. Rearranging the equations for the individual Fourier cosine components of (19), we have

$$A_n + g_n \sum_{k=0}^{\infty} A_k + h_n \sum_{k=0}^{\infty} (2k+1) A_k = 0, \tag{22}$$

for all positive integers n, where $g_n = \tilde{B}_n/\tilde{D}_n$ and $h_n = \tilde{C}_n/\tilde{D}_n$, with

$$\begin{aligned}
\tilde{B}_n &= \frac{4\alpha(\alpha^2-1)}{\pi(\alpha^2+4n^2)}, \qquad \tilde{C}_n = -\frac{4i\gamma\lambda\alpha}{\pi(\alpha^2+4n^2)}, \\
\tilde{D}_n &= -\frac{\lambda^2}{2n} + 4i\lambda\gamma(2n+1) + (4n^2-1),
\end{aligned} \tag{23}$$

$\lambda = \omega/\Omega$ being a dimensionless frequency. Mode coupling occurs purely through the boundary layer terms g_n and h_n in the corner regions where the bubble meets the walls. Without these terms, one recovers the 2D analogy of the surface mode dynamics for a spherical bubble in bulk fluid, which remains unexcited by a long wavelength forcing.[33]

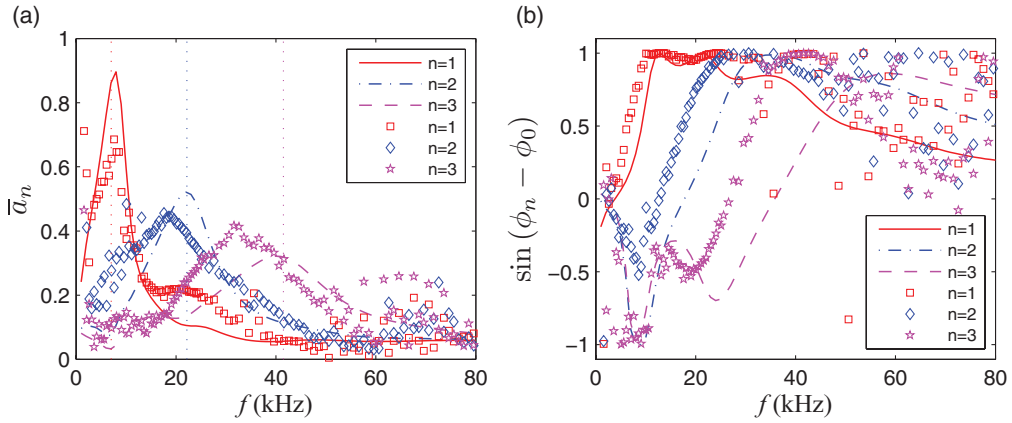

FIG. 7. (a) Relative amplitudes $\bar{a}_n$ and (b) sine of relative phase angles $\phi_n - \phi_0$ of the first three even surface modes. The symbols correspond to experimentally measured values for a nearly hemicylindrical bubble and the solid lines are predicted by the theory. Vertical lines indicate the undamped resonance frequencies of corresponding surface modes of free cylindrical bubbles in bulk.

In order to determine the strength of the surface mode amplitudes relative to the volume mode, we solve (22) in conjunction with (14), for $A_{n\geq 1}$ in terms of A_0. Truncating the series at $n = N$, we obtain an overdetermined system of $N + 1$ equations for the N unknowns A_1 through A_N,

$$A_n + g_n \sum_{k=0}^{N} A_k + h_n \sum_{k=0}^{N} (2k+1) A_k = 0, \tag{24a}$$

$$\sum_{n=0}^{N} A_n = 0\,. \tag{24b}$$

To accommodate the pinning condition (14), we first write $\sum_0^N A_n = K\delta^2$ with a constant $K = O(1)$ and verify that the results are not sensitive to the choice of K, including setting $K = 0$. Equation (24) may be concisely written as $G_{in}A_n = A_0 f_i$, where G_{in} encodes N dynamical equation (24a) and kinematic condition (24b), and f_i contains only terms of (24a) with prefactor A_0. The Fourier mode amplitudes of the flow field A_n may now be solved for as scalar multiples of A_0 by a least squares minimization of the norm of the residual $\|\boldsymbol{G}.\boldsymbol{A} - A_0\boldsymbol{f}\|_2$.

Using these A_n, we decompose the bubble outline $\zeta(\theta)$ in (16) into its Fourier cosine components ζ_n and obtain surface mode shape amplitudes a_n and phases ϕ_n, as given in (1),

$$\zeta(\theta) = \sum_{n=0}^{N} \zeta_n \cos 2n\theta = \sum_{n=0}^{N} a_n e^{i\phi_n} \cos 2n\theta\,. \tag{25}$$

Relative amplitudes $\bar{a}_n = a_n/a_0$ and phases $\phi_n - \phi_0$ can now be compared to experiment (see Figs. 7(a) and 7(b)). The peaks of the relative amplitude curves occur near the resonance frequencies for a bubble in free space $\Omega_n = \Omega\sqrt{2n(4n^2-1)}$. The main features of the amplitude and phase curves are reproduced consistently for each surface mode and are a consequence of the surface mode coupling to the volume mode as well as to each other. The widths of the amplitude curves are greater than expected from the damping coefficient γ alone—it must be noted here that the oscillator equation (19) contains indirect contributions to damping from the vortical boundary layer flow, leading to higher effective damping. Such contributions were previously noted for shape oscillations of spherical bubbles by Prosperetti[40] and in the context of sonoluminescing bubbles.[41] The shape of the curves is not very sensitive to the choice of truncation N, though larger N leads to smaller residuals, i.e., better approximations of (14). The remaining discrepancies can be attributed to (i) the relatively large size of δ in experiment—expansions in this theory generally demand $n\delta \ll 1$, but for the frequencies in the range considered we have only $n\delta \lesssim 0.4$; (ii) neglected axial

oscillations of the bubble may lead to shifts in the azimuthal resonance frequencies[38,39] and minor components of 3D flow (these effects could become stronger for bubbles of larger axial extent D, as smaller axial wavenumbers become accessible); (iii) the results are rather sensitive to changes in bubble rest shape: While the theory is compared here to experimental data for bubbles very close to hemicylindrical shape, the resonances of slightly smaller (less than hemicylindrical) bubbles show improved agreement.

The theory provides the full oscillatory flow field at any frequency, which is required in the calculation of the steady streaming flow. At lower frequencies, where there are significant contributions by individual surface modes, the flow patterns are dominated by a mixed mode streaming from the bubble (as seen in experiment, Fig. 5). At higher frequencies, where the oscillatory flow is dominated by the monopole, streaming along the wall becomes important.

IV. APPLICATION: OPTIMIZATION OF MIXING

With a quantitative understanding of the way flow patterns change when driving frequency f is altered, we can tailor the streaming flows through tuning the frequency to fit a specific purpose in a microfluidic application. Here we demonstrate mixing enhancement through frequency modulation.

Homogeneous mixing of samples and reagents is an essential preparation step for biological and chemical reactions in μTAS (micro total analysis systems), but it is hindered by the laminar character of the flow (note that our steady-flow Reynolds number remains small throughout). Mixers based on microbubble steady streaming have been demonstrated in various set-ups,[19] including practical applications such as DNA hybridization.[42] Most of the studies employed a single frequency driving strategy.[19,23,42]

A bubble microstreaming set-up like ours should favor mixing because, when superimposed on a directional flow, it forces fluid elements through a narrow gap between the bubble and vortex streamlines,[20,21] stretching and folding the fluid elements in the process. However, we show here that continuous low-frequency driving with a "fountain" flow does *not* lead to the most effective mixing.

To illustrate this concept, we monitor the distribution of fluorescent particles (radius $r_p = 50$ nm, Life Technologies) in a T-junction mixer[43] with a single oscillating bubble. Two streams of the same liquid, one with fluorescent particles and one without, are injected (right to left) through the T-junction with a bubble downstream of the junction, merging into a single Poiseuille flow in the main channel of mean speed $\bar{u}_p$ (Figs. 8(a)–8(d)). When the bubble is at rest, the particle distribution clearly shows laminar flow and non-mixing behavior (Fig. 8(a)). At a low driving frequency, the primary "fountain" of the steady streaming combines with the Poiseuille flow to a quasi-2D steady flow described before in sorting applications.[20,21] However, such a flow is not entirely effective in mixing the fluids across the channel width (observe the uneven intensity distribution downstream of the bubble in Fig. 8(b)). Can modulations of the driving frequency enhance the degree of mixing?

To answer this question we quantify the mixing quality using the fluorescence signal c from a window of size 250 μm $\times$ 250 μm centered 575 μm downstream of the bubble, which is indicated by a square box in Fig. 8(a). Various quantifications of mixing have been described in the literature; we employ (i) a coefficient of variation of the grayscale signal[44,45] $\sigma(c)/\bar{c}$ as a fast and simple measure and (ii) the mix-variance[46] $\Phi^2(c-\bar{c})$ as a more sophisticated measure, which takes into account the advection pattern of the fluid on all length scales within our window of interest. Note that the Stokes-Einstein diffusion coefficient of our nanoparticles is so small ($D_{SE} = k_B T/(6\pi\mu r_p)$ $\approx 2.4 \times 10^{-12}\mathrm{m}^2\mathrm{s}^{-1}$) that the stretching-and-folding patterns of bright and dark fluid remain visible throughout our field of view, so that we can evaluate and optimize the mixing effect of the flow field advection independent of diffusion effects. Note also that our flow is a practically relevant, continuous-throughput flow (rather than a flow in a confined space, where the fluid elements never leave the volume)—there is only finite time available for mixing.

We first consider the effect of breaking up the steady flow through low-frequency duty cycling: the ultrasound of fixed amplitude and frequency is turned on and off alternately for fixed time intervals $\tau \gg 1/f$. As seen in Figs. 8(c), 8(e), and 8(f) this strategy does improve mixing in both measures, if τ is large enough (note $\tau = 0$ is the continuous case). Duty cycling is advantageous

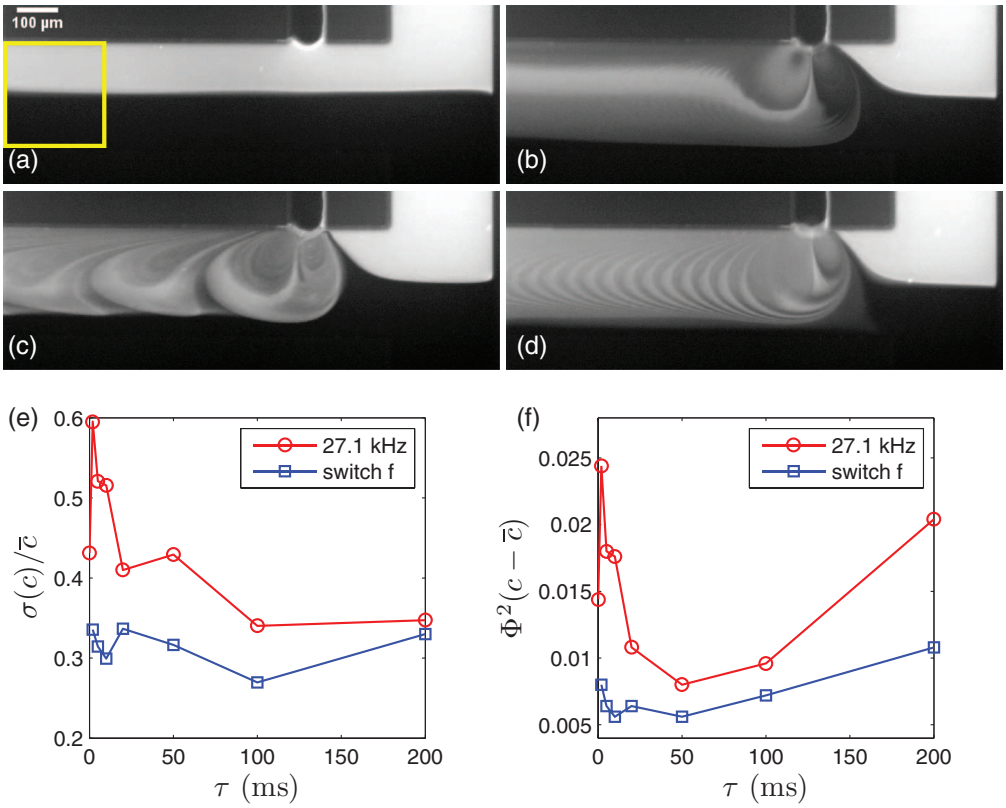

FIG. 8. Mixing in microstreaming flows combining a steady channel flow (right to left) with bubble streaming at different driving modulation: (a) bubble is not excited; (b) bubble is driven continuously at 27.1 kHz; (c) bubble is alternately driven at 27.1 kHz and undriven ($\tau = 50$ ms); (d) bubble is alternately driven at 27.1 kHz and 91.3 kHz, for intervals of $\tau = 5$ ms; (e) coefficient of variation of the grayscale signal $\sigma(c)/\bar{c}$; (f) mix-variance $\Phi^2(c-\bar{c})$ calculated based on the sampling window indicated as a square box in (a), as a function of interval time τ. For both measures used here, smaller values indicate better mixing and the frequency-switching strategy provides superior mixing throughout.

because, during the "off" part of the cycle, new unmixed fluid enters the region that—during the "on" part of the cycle—is taken up by the streaming vortices, quickly stretching out this fluid into thin bands. This mixed region is then advected downstream when the driving is turned off again, leading to bright and dark fluid regions distributed across the entire channel height $0 \le z \le H$. This reduces the mix-variance measure in particular, which emphasizes uniformity on large length scales.[46] With continuous driving (as in Fig. 8(b)), this process cannot happen.

Maximum efficiency is expected when the time scale τ allows transport of unmixed fluid across an entire bubble diameter (i.e., a scale of w). If τ is much smaller, the liquid distribution does not change much during the intervals of no driving; if it is much larger, unmixed fluid flows by without being mixed. Thus, we expect the best mixing close to $\tau_p = w/\bar{u}_p$. In our experiments, with $w = 80\mu$m and $\bar{u}_p \approx 1.3$ mm/s, we find $\tau_p \approx 60$ ms, in close agreement with the best mixing values in Figs. 8(e) and 8(f). The mix-variance, in particular, detects this minimum very consistently at different driving amplitudes (data not shown).

However, mixing can be further improved by alternating streaming between lower and higher frequencies. We again adopt time intervals of length τ, but now we switch between $f = 27.1$ kHz and $f = 91.3$ kHz driving at comparable amplitude. The Poiseuille advection part of the cycle is then replaced by a different bubble streaming advection, which also redistributes the fluid, but does so on a shorter time scale, as the flow speed of streaming is faster. As seen in Fig. 8(d), the short time scales lead to a finer structure of stretching-and-folding stripes in the flow, together with the desired large-scale mixing across the z-direction of the channel. The mixing quality is thus significantly enhanced using this method and the finer striations of the fluid are desirable as the time scale of

eventual diffusive mixing is governed by their length scale. Note that this approach only works when the switch frequencies belong to different modes of oscillation and thus substantially different flow fields. With the analysis of bubble interfacial oscillations detailed above, such a mixing strategy can be designed in advance: In our example, we have chosen 27.1 and 91.3 kHz to maximize the difference in flow fields between the cycles and thus the mixing quality. The mixing measures in Figs. 8(e) and 8(f) for frequency switching indicate better mixing throughout and additionally show a second minimum at a much smaller time scale τ_f. By the same arguments as above, we estimate this time as $\tau_f = w/u_s$, where the characteristic velocity of streaming[20] replaces that of the Poiseuille velocity. The streaming velocity near the bubble surface in our experiments is $u_s \approx 10$ mm/s, resulting in $\tau_f \approx 8$ ms, again in close agreement with the location of this second minimum. Apart from the obvious advantage of mixing on smaller time scales, the more accurate mix-variance criterion also rates this minimum at τ_f as better in mixing quality. Note that the estimates of τ_p and τ_f rely on effective averaging over the oscillatory flow during a modulation time interval. As $\tau f > 50$ even for the shortest τ employed in our experiments, this time scale separation is accurately fulfilled.

V. CONCLUSIONS

The present work advances research towards a quantitative description of microstreaming from a semi-cylindrical oscillating bubble attached to a wall, experimentally measuring as well as modeling the oscillation modes of the bubble interface, which are an indispensable input for the calculation of the mixed-mode streaming relevant in practical applications. It is shown that the relative amplitudes of azimuthal surface modes to the volume mode provide a robust measure and predictive characteristic of the flow structure and that the features of the associated resonance structures in frequency space can be explained by asymptotic theory. Axial modes are both more strongly damped and more strongly decaying with distance from the bubble, leading to a flow field that can be described as two-dimensional. As frequency increases and higher-order shape modes significantly contribute to the bubble oscillation, more intricate vortex structures develop close to the bubble. The positions of the resonance peaks for the individual oscillation modes are well approximated by the expected resonance frequencies of free-bubble shape modes. However, the shape of the peaks (height and width) can only be understood through the coupling of different modes owing to the viscous effects in the boundary layers that govern the flow near the bubble interface and the wall. The relatively wide peaks help explain the robust flow field response obtained from bubbles in experiment, where an accurate fine-tuning of frequencies is generally unnecessary and frequency drift does not compromise the flows.

In describing the frequency ranges of substantially different flow patterns, the theory furthermore provides guidance for experiments seeking to alter the appearance of the flow field to suit particular applications. Specifically, we show that knowing the frequency dependence of the streaming flow field helps in optimizing micromixing efficiency through frequency modulation, as a strong change in the character of the flow over a modulation cycle enhances mixing considerably. These conclusions are robust with respect to the way mixing efficiency is quantified. Future work will aim at deriving the far-field streaming flows directly from the bubble interface modes described here, thus completing a theoretical description of a complex streaming phenomenon that has proved useful in a large number of applications ranging from transport and force actuation to microscale sorting.

[1] J. Friend and L. Yeo, "Microscale acoustofluidics: Microfluidics driven via acoustics and ultrasonics," Rev. Mod. Phys. **83**, 647–704 (2011).
[2] T. Laurell, F. Petersson, and A. Nilsson, "Chip integrated strategies for acoustic separation and manipulation of cells and particles," Chem. Soc. Rev. **36**, 492–506 (2007).
[3] T. Franke, A. R. Abate, D. A. Weitz, and A. Wixforth, "Surface acoustic wave (SAW) directed droplet flow in microfluidics for pdms devices," Lab Chip **9**, 2625–2627 (2009).
[4] T. Franke, S. Braunmüller, L. Schmid, A. Wixforth, and D. Weitz, "Surface acoustic wave actuated cell sorting (SAWACS)," Lab Chip **10**, 789–794 (2010).
[5] L. Yeo and J. Friend, "Ultrafast microfluidics using surface acoustic waves," Biomicrofluidics **3**, 012002 (2009).
[6] M. Tan, J. Friend, and L. Yeo, "Microparticle collection and concentration via a miniature surface acoustic wave device," Lab Chip **7**, 618–625 (2007).
[7] N. Riley, "Steady streaming," Annu. Rev. Fluid Mech. **33**, 43–65 (2001).

[8] N. Riley, "Acoustic streaming," Theor. Comput. Fluid Dyn. **10**, 349–356 (1998).
[9] N.-T. Nguyen and R. M. White, "Acoustic streaming in micromachined flexural plate wave devices: numerical simulation and experimental verification," IEEE Trans. Ultrason. Ferroelectr. Freq. Control **47**, 1463–1471 (2000).
[10] B. R. Lutz, J. Chen, and D. T. Schwartz, "Microfluidics without microfabrication," Proc. Natl. Acad. Sci. U.S.A. **100**, 4395–4398 (2003).
[11] P. Marmottant and S. Hilgenfeldt, "Controlled vesicle deformation and lysis by single oscillating bubbles," Nature (London) **423**, 153–156 (2003).
[12] C. Lin, Y. Lai, H. Liu, and A. Wo, "Microvortices and recirculating flow generated by an oscillatory microplate for microfluidic applications," Appl. Phys. Lett. **93**, 133503 (2008).
[13] C.-M. Lin, H.-P. Liu, Y.-S. Lai, C.-C. Tseng, C.-Y. Chen, and A. Wo, "Micromixing via recirculatory flow generated by an oscillatory microplate," Microfluid. Nanofluid. **11**, 167–176 (2011).
[14] B. R. Lutz, J. Chen, and D. T. Schwartz, "Microscopic steady streaming eddies created around short cylinders in a channel: Flow visualization and stokes layer scaling," Phys. Fluids **17**, 023601 (2005).
[15] B. R. Lutz, J. Chen, and D. T. Schwartz, "Hydrodynamic tweezers: 1. Noncontact trapping of single cells using steady streaming microeddies," Anal. Chem. **78**, 5429–5435 (2006).
[16] J. A. Rooney, "Hemolysis near an ultrasonically pulsating gas bubble," Science **169**, 869–871 (1970).
[17] D. Miller, "Particle gathering and microstreaming near ultrasonically activated gas-filled micropores" J. Acoust. Soc. Am. **84**, 1378–1387 (1988).
[18] P. Marmottant and S. Hilgenfeldt, "A bubble-driven microfluidic transport element for bioengineering," Proc. Natl. Acad. Sci. U.S.A. **101**, 9523–9527 (2004).
[19] D. Ahmed, X. Mao, B. K. Juluri, and T. J. Huang, "A fast microfluidic mixer based on acoustically driven sidewall-trapped microbubbles," Microfluid. Nanofluid. **7**, 727–731 (2009).
[20] C. Wang, S. Jalikop, and S. Hilgenfeldt, "Size-sensitive sorting of microparticles through control of flow geometry," Appl. Phys. Lett. **99**, 034101 (2011).
[21] C. Wang, S. Jalikop, and S. Hilgenfeldt, "Efficient manipulation of microparticles in bubble streaming flows," Biomicrofluidics **6**, 012801 (2012).
[22] M. Patel, A. Tovar, and A. Lee, "Lateral cavity acoustic transducer as an on-chip cell/particle microfluidic switch," Lab Chip **12**, 139–145 (2012).
[23] S. Wang, Z. Jiao, X. Huang, C. Yang, and N. Nguyen, "Acoustically induced bubbles in a microfluidic channel for mixing enhancement," Microfluid. Nanofluid. **6**, 847–852 (2009).
[24] W. L. Nyborg, "Acoustic streaming near a boundary," J. Acoust. Soc. Am. **30**, 329–339 (1958).
[25] B. Davidson and N. Riley, "Cavitation microstreaming," J. Sound Vib. **15**, 217–233 (1971).
[26] M. Longuet-Higgins, "Viscous streaming from an oscillating spherical bubble," Proc. R. Soc. London, Ser. A **454**, 725–742 (1998).
[27] S. A. Elder, "Cavitation microstreaming," J. Acoust. Soc. Am. **31**, 54–64 (1959).
[28] P. Tho, R. Manasseh, and A. Ooi, "Cavitation microstreaming patterns in single and multiple bubble systems," J. Fluid Mech. **576**, 191–233 (2007).
[29] P. Marmottant, J. P. Raven, H. Gardeniers, J. G. Bomer, and S. Hilgenfeldt, "Microfluidics with ultrasound-driven bubbles," J. Fluid Mech. **568**, 109–118 (2006).
[30] J. Xu and D. Attinger, "Acoustic excitation of superharmonic capillary waves on a meniscus in a planar microgeometry," Phys. Fluids **19**, 108107 (2007).
[31] J. C. McDonald, D. C. Duffy, J. R. Anderson, D. T. Chiu, H. Wu, O. J. A. Schueller, and G. M. Whitesides, "Fabrication of microfluidic systems in poly(dimethylsiloxane)," Electrophoresis **21**, 27–40 (2000).
[32] W. Rasband, ImageJ, U. S. National Institutes of Health, Bethesda, Maryland, USA, 1997-2012, see http://imagej.nih.gov/ij/.
[33] M. Plesset and A. Prosperetti, "Bubble dynamics and cavitation," Annu. Rev. Fluid Mech. **9**, 145–185 (1977).
[34] T. G. Leighton, *The Acoustic Bubble* (Academic, 1997).
[35] D. Lyubimov, T. Lyubimova, and S. Shklyaev, "Behavior of a drop on an oscillating solid plate," Phys. Fluids **18**, 012101 (2006).
[36] B. Vukasinovic, M. Smith, and A. Glezer, "Dynamics of a sessile drop in forced vibration," J. Fluid Mech. **587**, 395–423 (2007).
[37] I. Fayzrakhmanova, A. Straube, and S. Shklyaev, "Bubble dynamics atop an oscillating substrate: Interplay of compressibility and contact angle hysteresis," Phys. Fluids **23**, 102105 (2011).
[38] A. Sanz, "The influence of the outer bath in the dynamics of axisymmetric liquid bridges," J. Fluid Mech. **156**, 101–140 (1985).
[39] A. Sanz and J. Diez, "Non-axisymmetric oscillations of liquid bridges," J. Fluid Mech. **205**, 503–521 (1989).
[40] A. Prosperetti, "Viscous effects on perturbed spherical flows," Q. Appl. Math. **35**, 339–352 (1977).
[41] S. Hilgenfeldt, D. Lohse, and M. Brenner, "Phase diagrams for sonoluminescing bubbles," Phys. Fluids **8**, 2808 (1996).
[42] R. Liu, R. Lenigk, R. Druyor-Sanchez, J. Yang, and P. Grodzinski, "Hybridization enhancement using cavitation microstreaming," Anal. Chem. **75**, 1911–1917 (2003).
[43] D. Gobby, P. Angeli, and A. Gavriilidis, "Mixing characteristics of t-type microfluidic mixers," J. Micromech. Microeng. **11**, 126–132 (2001).
[44] P. Garstecki, M. Fischbach, and G. Whitesides, "Design for mixing using bubbles in branched microfluidic channels," Appl. Phys. Lett. **86**, 244108 (2005).
[45] T. Frommelt, M. Kostur, M. Wenzel-Schäfer, P. Talkner, P. Hänggi, and A. Wixforth, "Microfluidic mixing via acoustically driven chaotic advection," Phys. Rev. Lett. **100**, 034502 (2008).
[46] G. Mathew, I. Mezić, S. Grivopoulos, U. Vaidya, and L. Petzold, "Optimal control of mixing in stokes fluid flows," J. Fluid Mech. **580**, 261–281 (2007).